nature portfolio

https://doi.org/10.1038/s41586-021-03733-7

Supplementary information

Mobility gradients yield rubbery surfaces on top of polymer glasses

In the format provided by the authors and unedited

Supplementary information for

Mobility Gradients Yield Rubbery Surfaces on top of Polymer Glasses

Zhiwei Hao[1,†], Asieh Ghanekarade[2,†], Ningtao Zhu[1], Katelyn Randazzo[3], Daisuke Kawaguchi[5], Keiji Tanaka[5], Xinping Wang[1], David S. Simmons[2,*], Rodney D. Priestley[3,4,*], and Biao Zuo[1,*]

Affiliations:

[1] Department of Chemistry, Key Laboratory of Surface & Interface Science of Polymer Materials of Zhejiang Province, National Engineering Lab for Textile Fiber Materials and Processing Technology (Zhejiang), Zhejiang Sci-Tech University, Hangzhou, China.

[2] Department of Chemical and Biomedical Engineering, University of South Florida, Tampa, Florida, United States.

[3] Department of Chemical and Biological Engineering, Princeton University, Princeton, New Jersey, United States.

[4] Princeton Institute for the Science and Technology of Materials, Princeton University, Princeton, New Jersey, United States.

[5] Department of Applied Chemistry, Center for Polymer Interface and Molecular Adhesion Science, Kyushu University, Fukuoka, Japan.

[*]Correspondence to: dssimmons@usf.edu (for DSS); rpriestl@princeton.edu (for RDP)
chemizuo@zstu.edu.cn (for BZ)

[†]These authors contributed equally to this work.

This PDF file includes:

Supplementary Theoretical Development

In order to obtain a leading-order mean field theory of of the emergence of an interfacial transient elastomeric domain, we employ a minimal dynamical model of a polymer chain: in the bulk, the chain obeys sub-diffusive Rouse dynamics at all times less than the Rouse time of the whole chain and exhibits a restoration of diffusive dynamics at longer times. We do not explicitly model the segmental relaxation process itself, although we treat the segmental alpha relaxation time τ as setting the rate of Rouse subdiffusion:

$$\left\langle r^2(t)\right\rangle = \left(\frac{t}{\tau}\right)^{1/2} \qquad t < \tau_{\text{Rouse}} \tag{1}$$

We consider the motion of such a chain, of length n, placed near the surface of a film within the surface gradient in segmental relaxation time, $\tau(z,T)$. Prior work has shown this gradient to be of a double exponential form[1–9]

$$\tau(z,T) = \tau_{bulk}(T)\exp\left[-A(T)\exp\left(-\frac{z}{\xi}\right)\right] \tag{2}$$

where $\tau_{bulk}(T)$ is the bulk segmental relaxation time at a temperature T, $A(T)$ is a temperature-dependent parameter that sets the magnitude of the gradient at temperature T, and ξ is a range parameter that is at most weakly temperature-dependent. Prior work has established the temperature variation of $A(T)$[1,10,11] :

$$A(T) = \varepsilon_0 \ln\frac{\tau_{bulk}(T)}{\tau^*} \tag{3}$$

Here ε_0 is a constant reflecting the fractional reduction in the activation barrier for segmental relaxation at the surface relative to bulk, and τ^* is an onset timescale for the segmental relaxation time gradient. In practice τ^* has a weak z-dependence that is relevant to quantitative prediction[Error! Bookmark not defined.], but here we treat this quantity as constant for the purposes of a leading-order treatment. Prior simulation results in this model suggest $\varepsilon \cong 0.8$, $\xi \cong 4$, and $\tau^* \cong 1\ \tau_{\text{LJ}}$. We employ these values below in making quantitative theory predictions[Error! Bookmark not defined..Error! Bookmark not defined.].

We now consider the mean square displacement of a segment at a distance z_1 from the surface. At short times, this segment obeys Rouse subdiffusion as in the bulk, albeit at a rate determined by the local relaxation time:

$$\left\langle r^2(z_1,t)\right\rangle = \left(\frac{t}{\tau(z_1)}\right)^{1/2} \tag{4}$$

However, at long times this segment's motion is constrained by a tether to a segment deeper in the film at position $z_2 > z_1$. We compute the number of segments in this tether by modeling it as a one-dimensional random walk from z_1 to z_2, with a reflecting boundary condition at $z = 0$. The expectation value $E\left[n(z_1 \to z_2)\right]$ for this number of steps is given via a first-passage analysis by the equation[12]

$$E\left[n(z_1 \to z_2)\right] = \frac{{z_2}^2 - {z_1}^2}{{a_z}^2} = \frac{{z_2}^2 - {z_1}^2}{a^2/3} \tag{5}$$

where a_z is the average step size in the z direction and a is the bond length. In the in-plane direction, this tether is a random walk obeying Gaussian chain statistics, and it thus has mean in-plane end-to-end length of

$$R_{\|}^2 = {a_{\|}}^2 n = \frac{2}{3}a^2 n \tag{6}$$

If we treat this mean end-to-end length as the in-plane length of the tether, we thus expect the mean square in-plane tether length to be equal to

$$R_{\|}^2(z_1,z_2) = 2\left({z_2}^2 - {z_1}^2\right) \tag{7}$$

Because Rouse subdiffusion of the segment at z_1 is innately faster than that at z_2 (because of the dynamical gradient in segmental relaxation times), beyond some time $t^*(z_1, z_2)$ the motion of the segment at z_1 will be restricted by this tether. This occurs approximately at the time t^* at which

$$\left\langle r^2\left(z_1, t^*(z_1,z_2)\right)\right\rangle = R_{\|}^2(z_1,z_2) + \left\langle r^2\left(z_2, t^*(z_1,z_2)\right)\right\rangle \tag{8}$$

At longer times, the segment at z_1 displaces at the same rate as the segment at z_2, since further motion of the segment at z_2 is now the rate limiting step for the segment at z_1.

$$\left\langle r^2(z_1,t)\right\rangle = \begin{cases} \left(\dfrac{t}{\tau(z_1)}\right)^{1/2} & t < t^*(z_1,z_2) \\ \left\langle r^2(z_2,t)\right\rangle + R_{\|}^2(z_1,z_2) & t \geq t^*(z_1,z_2) \end{cases} \tag{9}$$

The motion of the segment at z_2 is then further constrained by a yet deeper segment at z_3, such that at times longer than $t^*(z_2, z_3)$ its motion is likewise restricted. Similarly, that segment is restricted by a yet deeper segment, and so on. We thus have in general a recursive equation relating layers nearest the interface to layers deeper in the film:

$$\left\langle r^2(z_i,t)\right\rangle = \begin{cases} \left(\dfrac{t}{\tau(z_i)}\right)^{1/2} & t < t^*(z_i,z_j) \\ \left\langle r^2(z_j,t)\right\rangle + R_{\|}^2(z_i,z_j) & t \geq t^*(z_i,z_j) \end{cases} \tag{10}$$

with $t^*(z_i,z_j)$ defined as

$$\left\langle r^2\left(z_i, t^*(z_i,z_j)\right)\right\rangle = R_{\|}^2(z_i,z_j) + \left\langle r^2\left(z_j, t^*(z_i,z_j)\right)\right\rangle, \tag{11}$$

with

$$R_{\|}^2(z_i,z_j) = 2\left({z_j}^2 - {z_i}^2\right) \tag{12}$$

and where this relation must be satisfied for all $z_j > z_i$.

For a chain of finite length, this recursive relation can be solved by beginning at the position Z of the segment furthest from the interface and considering small sequential steps of size Δz nearer to the surface. The segment at Z displaces at all times less than the relaxation time of the full chain via the

Rouse scaling, because it is not tethered to anything deeper in thin film:

$$\left\langle r^2\left(t,Z\right)\right\rangle = \left(\frac{t}{\tau\left(z=Z\right)}\right)^{1/2} \quad \text{for all } t < \tau_{Rouse}. \qquad (13)$$

Each layer k closer to the surface then displaces according to equation (10), with $z_i = Z - k\Delta z$ and $z_j = Z - (k-1)\Delta z$. Since the fluid is not genuinely comprised of discrete layers, Δz can be made arbitrarily small to converge to the continuous limit. We determine Z for a chain of length n by employing equation (5) and determining the largest value $z = Z$ to which the mean first-passage number of steps from the surface (z = 0) is less than or equal to n:

$$Z = a\sqrt{\frac{n}{3}} \qquad (14)$$

The final consideration needed is the question of the effective Rouse time of the entire chain – the time of escape to fully diffusive dynamics. We approximate the chain Rouse time as the time at which the mean square displacement, average over all layers involved in the recursion relation above, is equal to the square gyration radius of the chain in the bulk ideal state, $a^2n/6$, where a is the bond length. We solve the system of recursive equations (10) numerically, identifying the crossover to diffusive dynamics via the above criterion numerically. We choose a small value of Δz and confirm that results are not sensitive to this choice in this low-Δz range.

Supplementary Simulation Methods

Simulations employ an attractive bead-spring model extended from the work of Kremer and Grest[13]. Within this model, non-bonded beads interact via the 12-6 Lennard-Jones (LJ) potential, with energy parameter ε = 1.0 and range parameter σ = 1.0, with interactions cut off at a distance of 2.5. Bonds are represented via the Finitely Extensible Nonlinear Elastic (FENE) potential, with K = 30, R_0 = 1.3, ε_{bond} = 0.8, and σ_{bond} = 1.0. This specific forcefield has been used to study dynamics in confined polymers in prior work[10,11] , with similar potentials employed in a large body of simulation work probing glass formation in polymers[2,14,15]. Simulations are performed in LAMMPS[16].

Data in the main text reflects simulations of chains of length 48 and 192 repeat units. These chains correspond to 0.6 and 2.3 times the entanglement length for this chain, which is reported to be 84 repeat units[17]. In each case, we simulate films of thickness approximately 26 σ, with lateral dimensions of $26\sigma_{LJ} \times 26\sigma_{LJ}$ to prevent any potential lateral confinement effects.

Simulations of the film comprised of 192-bead chain were performed as follows. Configurations were initiated by placing each chain on a lattice and then inserting chains randomly into the box. These configurations were then annealed isothermally at a reduced LJ temperature of 1.6 for 5 $\times 10^5$ τ_{LJ}, where τ_{LJ} is the LJ unit of time. Because the box size during this step is held constant and is considerably larger than required by the equilibrium density of the polymer, the polymer rapidly collapses into a film and then thermally anneals.

From here, we employed a recently published iterative quench protocol[15]. Specifically, we performed an isobaric temperature quench of the system described above to a temperature of 1.0, saving several temperatures along the way. We then isothermally equilibrated the configuration at each of these temperatures for 10^6 τ_{LJ}. We then performed a further quench from the annealed T = 1.0 sample, targeting a range over temperature over which the relaxation time is expected to increase by an order of magnitude. These temperatures were also annealed for 10^6 τ_{LJ}. This process was then iterated down to the lowest temperatures probed in the study.

The mean end-to-end reorientational relaxation time $\langle\tau_{ee}\rangle$ of the polymer in the film at the initial temperature of T = 1.6 is $10^{3.8}$ τ_{LJ} and is $10^{3.9}$ τ_{LJ} in an equivalent bulk simulation; the chain's end to end vector thus has sufficient time to relax over 60 times and for the chain reach conformational equilibrium in the initial high-temperature equilibration. With the protocol described above, the isothermal annealing period is at least 10 times $\langle\tau_{ee}\rangle$ down to a temperature of 0.714, and at least equal to $\langle\tau_{ee}\rangle$ down to a temperature of approximately 0.59. At lower temperatures reported, the annealing period is at least 10 times the segmental relaxation time, which recent work has demonstrated is more than sufficient to yield equilibrium glassy dynamics in this model[15]. Moreover, chain conformational statistics of the freely-jointed bead-spring polymer are approximately temperature invariant[18] (similarly to experimental polymers[19]), such that chain conformations are expected to reflect equilibrium behavior even at these lower temperatures. This approach is an extension of the recently developed Predictive Stepwise Quench (PreSQ) protocol[15].

In simulations of the subentangled 48-bead chain, this procedure is slightly modified. Instead of employing a fixed isothermal annealing period of 10^6 τ_{LJ} at each temperature, we anneal for a period of approximately $10\langle\tau_{ee}\rangle$ down to the lowest temperature at which this remains possible within a maximum annealing period of $10^6\tau_{LJ}$ (a temperature of 0.465). At lower temperatures we again employ a fixed annealing period of $10^6\tau_{LJ}$ and again ensure that equilibration times are at least 10 times the segmental relaxation time. The lowest temperature simulation performed through these simulations each required approximately 20 days of continuous simulation on a compute unit comprised of 8 3.0 GHz cores and a single GTX 1080 Ti GPU.

We analyze dynamics based on the mean square displacement $\langle r^2\rangle$, computed as

$$\left\langle r^2(t)\right\rangle = \frac{1}{S}\sum_{j}^{S}\frac{1}{N}\sum_{1}^{N}\left[r_i\left(s_j+t\right)-r_i\left(s_j\right)\right]^2$$

where s_j is the start time of observation, t is the time of displacement, N is the number of particles, and S is the number of start times over which $\langle r^2(t)\rangle$ is averaged. In order to analyze dynamics locally within the film, rather than averaging over all particles in the film, we average over subsets of segments selected based on their distance from the surface at time s. When reporting surface dynamics, we average only over segments that at time s are within a distance of 1 σ_{LJ} of the surface. When reporting mid-film dynamics, we average only over segments that at time s are in the central 1 σ_{LJ} of the film.

As described in the main text, in analyzing the data we consider the time dependent value of the scaling exponent λ in the relation $\langle r^2(t)\rangle \sim t^{\lambda}$. In the simulations Rouse and terminal regimes correspond to $\lambda \cong$ ½ and 1, respectively[20]. Unlike in creep, in $\langle r^2\rangle$ the entanglement regime does not correspond to a flat plateau, but rather to $\lambda \cong$ ¼ in the idealized infinite molecular weight limit. Here, however, we simulate finite chains comprised of 192 beads, which as noted above is only 2.3 times the reported entanglement molecular weight for this model. For finite molecular weight chains in simulation, observed whole chain values of γ computed in the entanglement regime are empirically slightly larger due to chain-end effects; the idealized value of ¼ is generally only observed in simulation if $\langle r^2(t)\rangle$ calculations are limited to only a few central beads (for example, 5 or 10 central beads) within the chain[17,20].

Because here we seek to quantify local dynamics within a narrow spatial region near or far from the surface of the film, an additional restriction to a small number of central repeat units would not yield sufficient statistical power. We thus analyze all beads and employ an empirical value of λ based on a calculation for the whole chain. To determine an appropriate whole-chain value of λ in this molecular weight range, we performed supplementary simulations of bulks samples comprised of 48-bead, 192-bead and 288-bead chains. As shown in Fig. S10., we find $\lambda \cong 2/5$ for dynamics in this crossover molecular weight range of light entanglement and we thus use this scaling as an empirical signature of entangled dynamics in these simulations. To better compare the results of this approach to experiment, we rescale $\langle r^2\rangle$ by this $t^{2/5}$ factor in the main text, as this normalized mean-square-displacement is expected to exhibit a plateau in the entanglement regime.

We additionally simulate and analyze dynamics for a subentangled 48-bead chain. Surface dynamics for this system are shown in the main text. Successful collapse of mid-film (bulk-like) data to a single time-temperature superposition (TTS) master curve is shown in Fig. S12.

Supplementary Data

Materials: Mono-disperse PS was purchased from Polymer Source Co. ltd. (Canada), and the $[EIm]BF_4$ ionic liquid was supplied by Lanzhou Institute of Physical Chemistry, Chinese Academy of Sciences. The physical parameters of $[EIm]BF_4$ are listed in Tab. S1. The [EIm]BF4 is extremely stable at temperatures below 686 K. The zero saturated vapor pressure ensures the invariance of droplet volume and profile during the long-time experiments (also see evidences in Fig. S1). The high surface tension (γ_l) guarantees the formation of a hemisphere droplet (i.e., non-wetting state) atop the PS surface with a contact angle (θ) of 72 ° (see Fig. S1), which creates considerable upward pulling force ($\gamma_l \sin\theta$) at the three-phase line to deform the surface (see Fig. 1 in the main text). As well, since the $[EIm]BF_4$ is water-soluble, it is immiscible with PS, a hydrophobic polymer. No interfacial swelling or plasticization effects were observed with PS (Figs. S2-S4). These characteristics render $[EIm]BF_4$ a good testing liquid for our creep experiments at the PS surface at a temperature ranging from 320 to 390 K.

Tab. S1. Physical parameters of [EIm]BF4

Sample	Water Solubility	Surface tension (298 K)	Saturated vapor pressure	Decomposition temperature
1-ethyl-3-methylimidazolium tetrafluoroborate ([EIm]BF 4)	Good	49 mN/m	~ 0	686 K

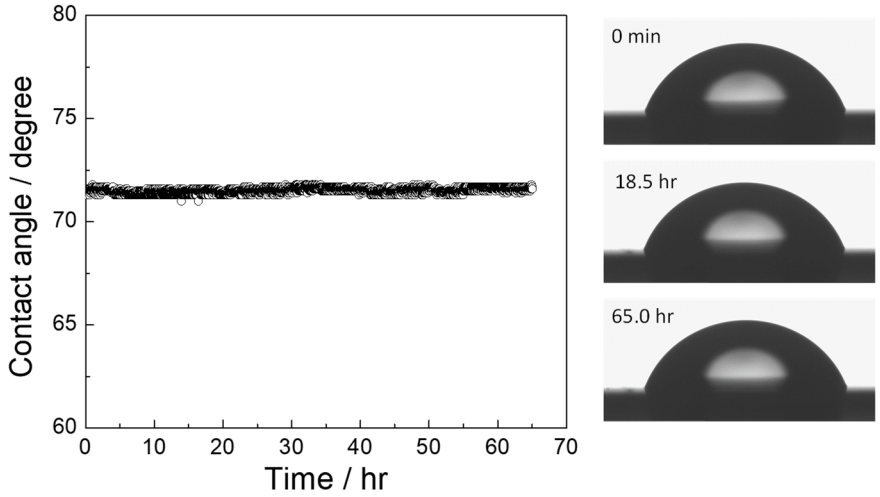

Fig. S1. (a) Time evolution of contact angle values of [EIm]BF4 ionic liquid on PS surface; (b) images showing the unaltered droplet profiles with time (T = 385 K). It is clear that the contact angle values and profile of the liquid droplet did not vary with time, ensuring a long-time creep experiment on polymer surface.

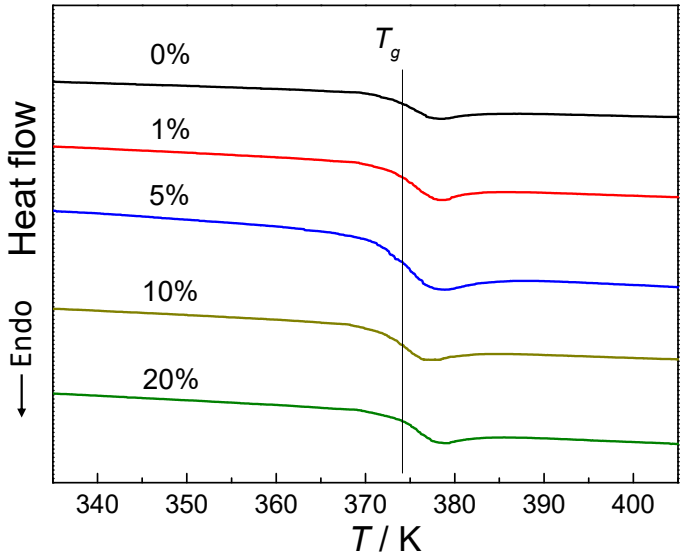

Fig. S2. (a) Differential scanning calorimetry (DSC) curves showing the unchanged T_g of the PS blended with [EIm]BF4. This means that the [EIm]BF4 does not plasticize PS.

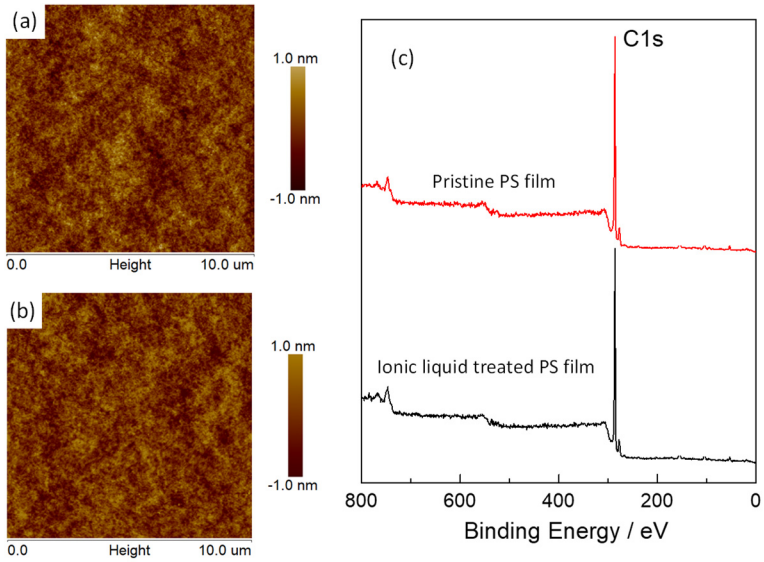

Fig. S3. (a, b) AFM topological images and (c) X-ray photoelectron spectroscopy (XPS) spectra for PS films before and after soaking in ionic liquid for 30 min at 385 K. The results showed that the polymer surface remains smooth and intact (panel a, b), and ionic liquid diffusions are not evident (panel c) after the films were contacted with ionic liquid.

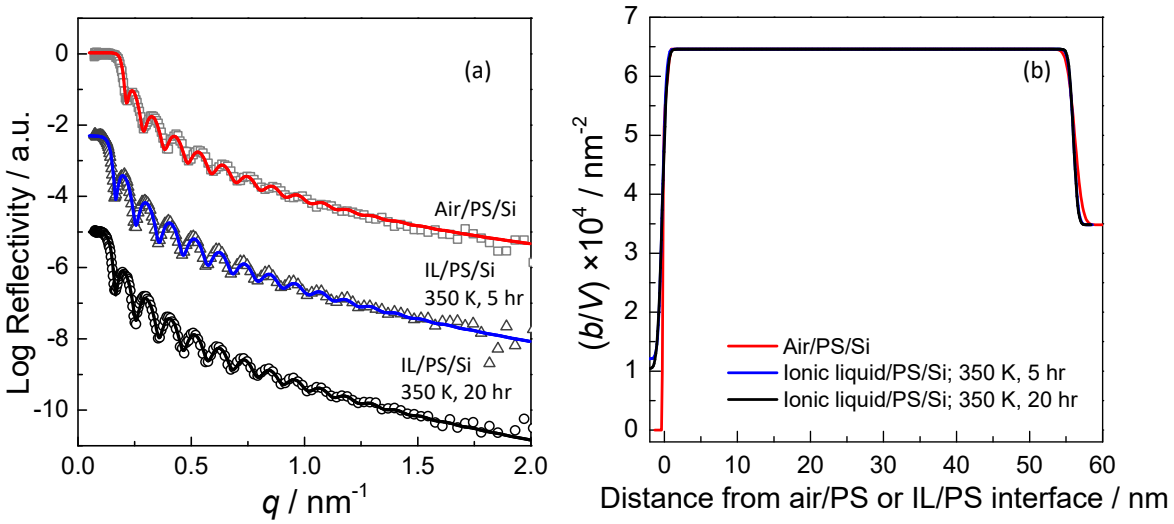

Fig. S4. (a) Neutron reflectivity for a deuterated PS film collected in air at room temperature and in a direct contact with the ionic liquid (IL) at 350 K after equilibrating for 5 and 20 hr. The solid curves represent the reflectivity calculated on the basis of the scattering length density (b/V) profiles shown in (b). For clarity, the curves in panel (a) are offset from one another on the y axis. Notably, except for slight differences in the top surface region due to the different b/V values for air and IL, the b/V profiles of PS films in air and in ionic liquid remain almost the same, and not any interfacial broadening between IL and PS was detected, as shown in panel (b). This means that IL molecules did not diffuse into the surface region of PS within our experimental time and temperature ranges.

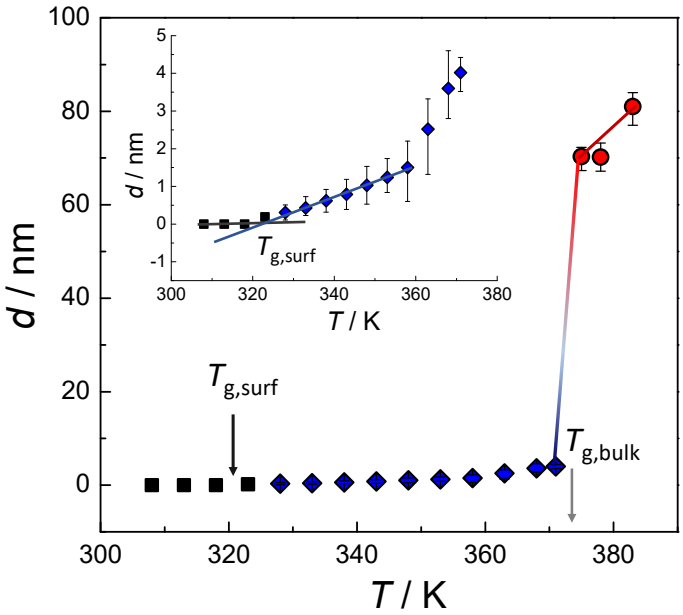

Fig. S5. Variation of the height of the wetting ridge (d) with temperature, showing the start of wetting ridge formation at $T_{g,surf}$ (about 320 K) and a sharp increase in d near $T_{g,bulk}$. The inset is the enlarged image showing the definition of $T_{g,surf}$. Below ca. 320 K, all deformation ceases, pointing to the vitrification of the surface layer below a surface T_g (i.e., $T_{g,surf.} \sim 320$ K). The d values in this figure were acquired after exposing the PS film surface to the ionic liquid for 200 s at various temperatures. Each data point represents averaged results from several measurements at a specific temperature.

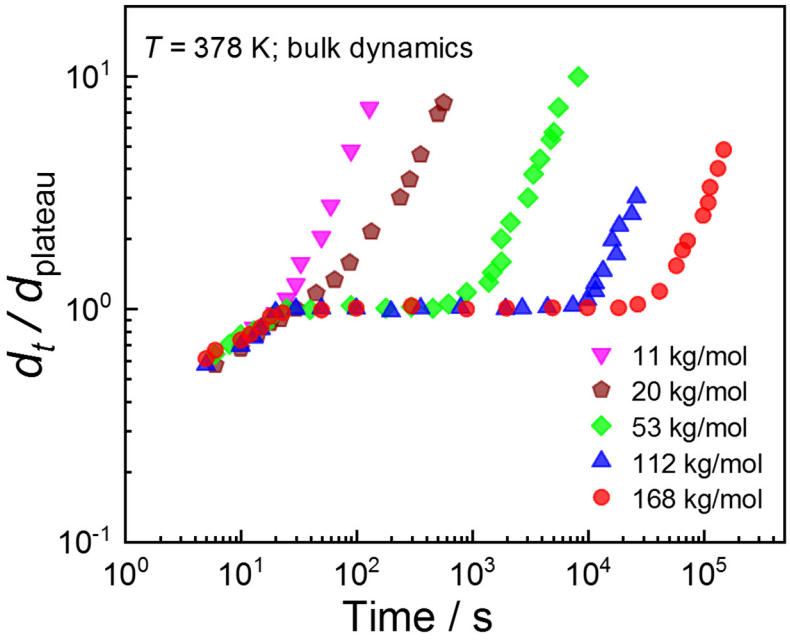

Fig. S6. Height of wetting ridge (d) as functions of creep time for PS film with various molecular weights (T = 378 K). The plateau disappears upon reducing the PS molecular weight to below 20 kg/mol, which is close to the entanglement molecular weight of PS (ca. 13 kg/mol).

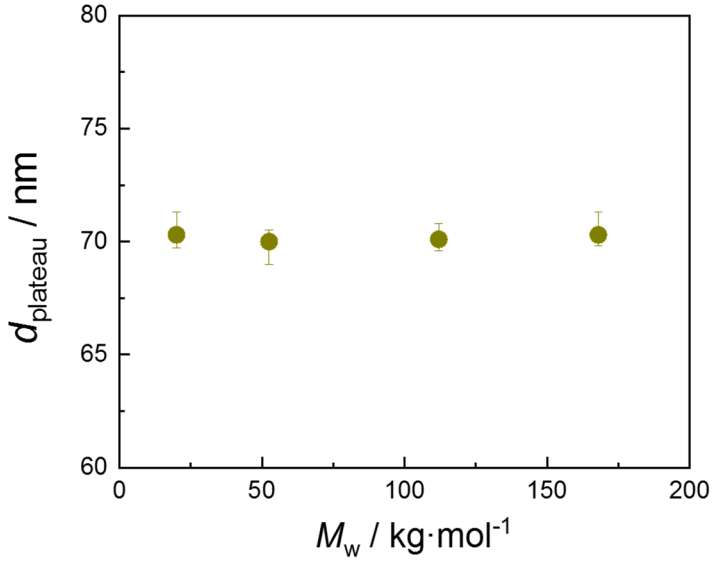

Fig. S7. Invariant height of wetting ridge at plateau region ($d_{plateau}$) with molecular weight of PS (T = 393 K). This further confirms the formation of a wetting ridge plateau region due to the rubbery plateau of PS, thus the relation: $d_{plateau} \sim D_R$. The rubbery compliance of PS is invariant with the chain length, as is $d_{plateau}$.

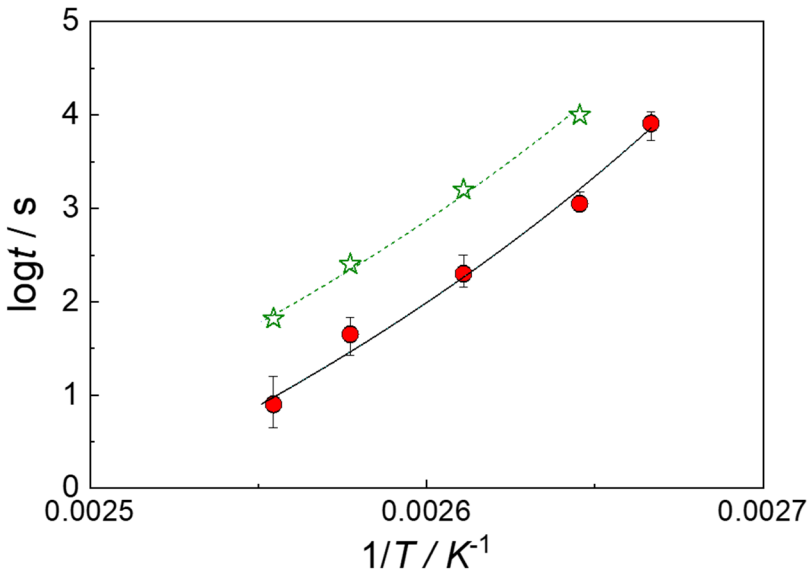

Fig. S8. Comparison of reptation times determined by torsional shear experiments and our nano-creep experiments. Red circles indicate the reptation time from wetting ridge deformation; hollow stars represent the reptation time constant deduced from zero shear viscosity and steady-state compliance obtained by torsional shear experiments in *J. Polym. Sci: A-2. Polym. Phys.* 1971, 9, 209-243. The values of the relaxation times are within an order of magnitude within each other. We believe that the difference is a reflection of the different measurement types and identification of the relaxation times. Importantly, the temperature dependence of the reptation times is the same from both the torsional shear experiments (literature data) and those from the wetting ridge deformation experiments, thus reflecting the same dynamics probed by the two experimental approaches.

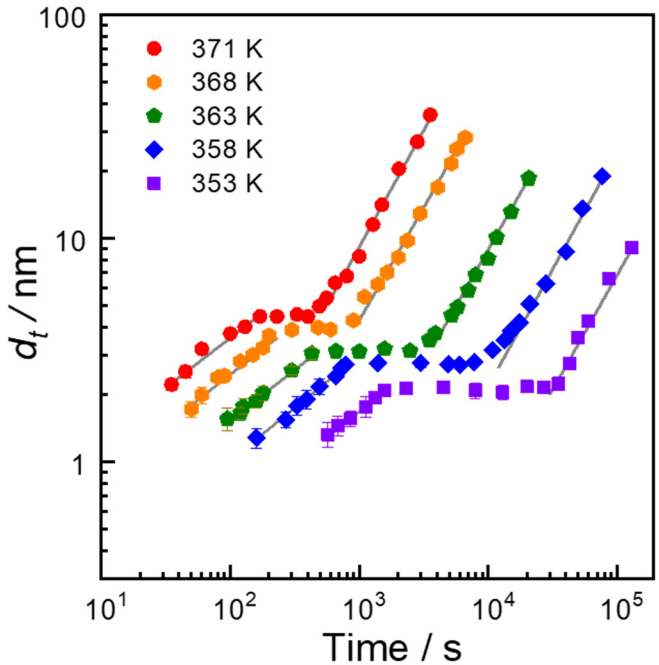

Fig. S9. Time evolution of the d_t at $T_{g,bulk} > T > T_{g,surf}$ (surface dynamics). The $d_{plateau}$ values decrease with decreasing temperature. This can be attributed to the decrement of the size of mobile surface region with cooling and is consistent with the simulation and theory findings. However, the variations in $d_{plateau}$ do not interfere with the determination of relaxation times at various temperatures.

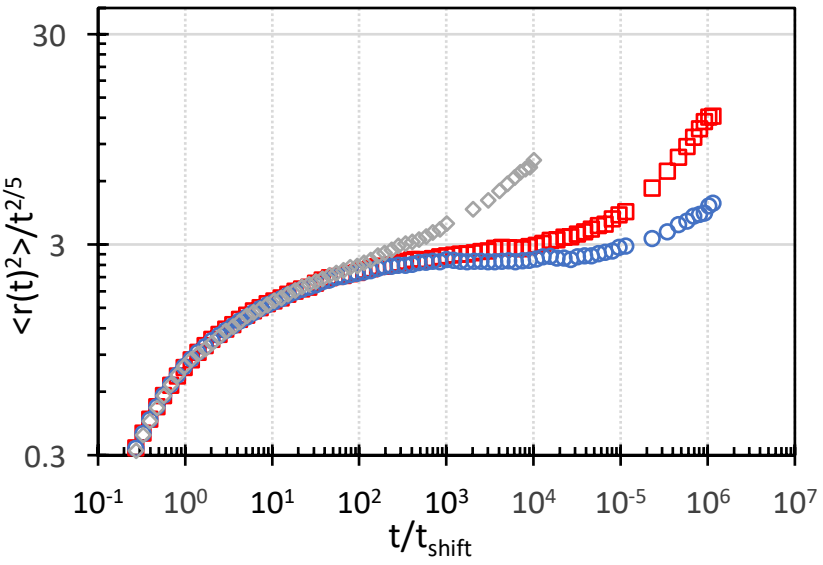

Fig. S10. Mean square displacement over $t^{2/5}$ for simulations of *bulk* systems comprised of 48-bead (grey diamonds), 192-bead (red squares) and 288-bead (blue circles) chains, plotted vs time, at a reduced temperature of 1.60. As seen here, chains with molecular weight of the 192-bead-spring polymer that we employ as a model entangled chain in the main text exhibit an entanglement plateau closely approaching the scaling $\langle r^2(t)\rangle \sim t^{2/5}$.

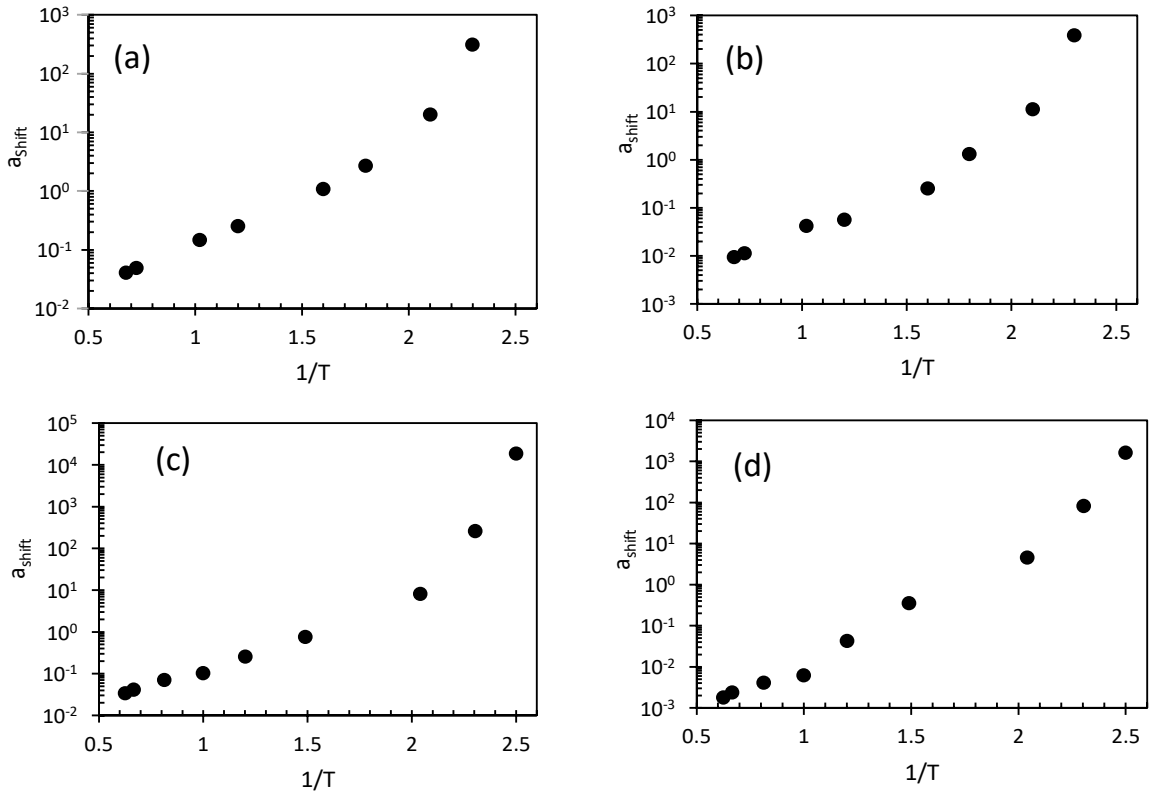

Fig. S11. Plot of *x*-axis (time- axis) shift parameter from simulation, in Lennard-Jones time units, vs inverse temperature, for (a) the 192-bead chain in the midfilm, (b) the 192-bead chain at the surface, (c) the 48-bead chain in the mid-film, and (d) 48-bead chain at the surface.

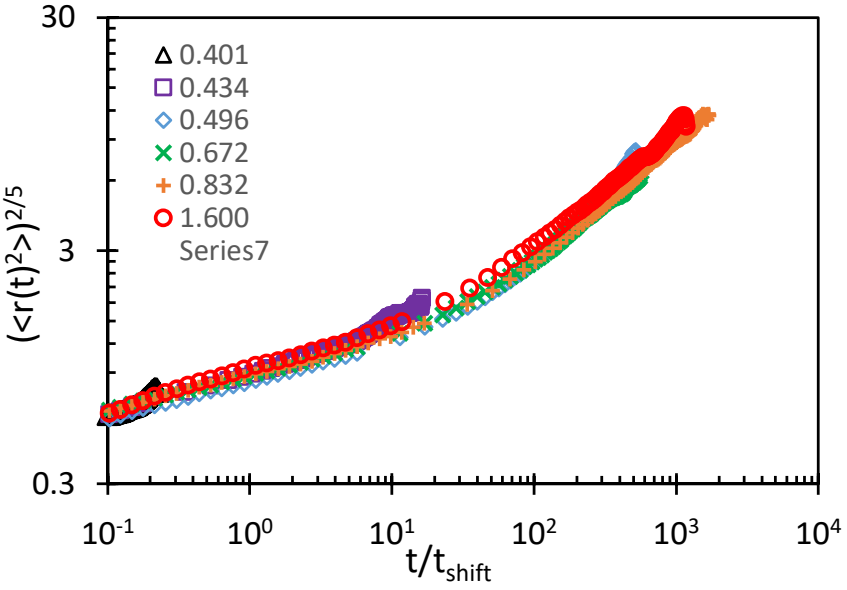

Fig. S12. Mean square displacement over $t^{2/5}$ for simulations of *mid-film* region of simulated films comprised of 48-bead chains, plotted vs time at the temperatures noted in the legend. The data collapse to a single master curve employing shift factors of t_{shift} and $<r^2>^{shift}$.

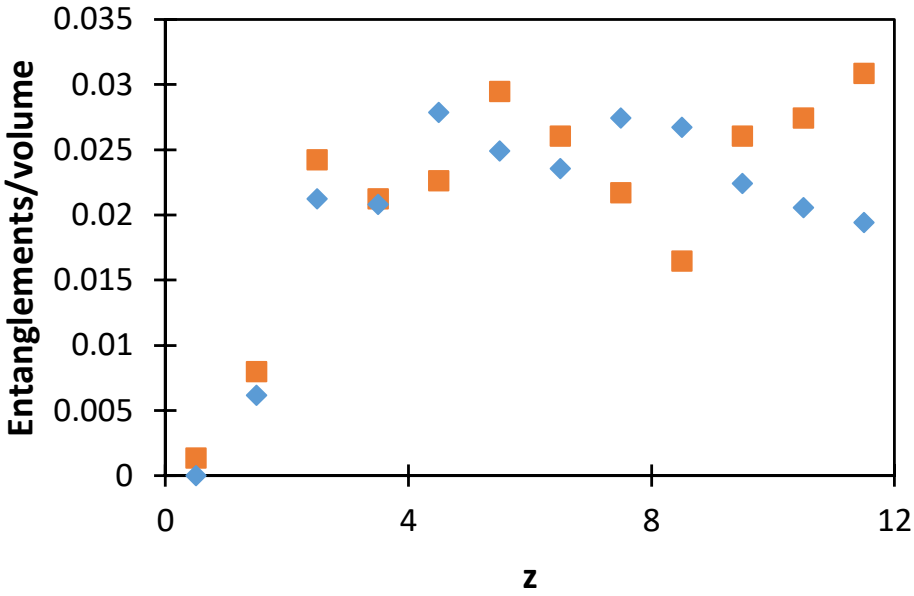

Fig. S13. Number of entanglements per volume as a function of depth in the film for 48-bead chain (orange squares) and 192-bead chain (blue circles), as computed via the Z1 algorithm[21,22]. Results are at the lowest reduced LJ temperature for each system: 0.402 for the 48-bead chain and 0.435 for the 192-bead chain. Results illustrate a depletion of entanglements (rather than an enhancement) at the film surface, such that topological entanglement cannot drive the interfacial transient elastomeric effect reported in the main text. As shown in the next figure, although the spatial density of topological entanglements is consistent between these two chain lengths (as expected), the shorter nature of the 48-bead chains renders them too short to form an entangled network due to insufficient number of entanglements per chain (the key order parameter for network formation via entanglement).

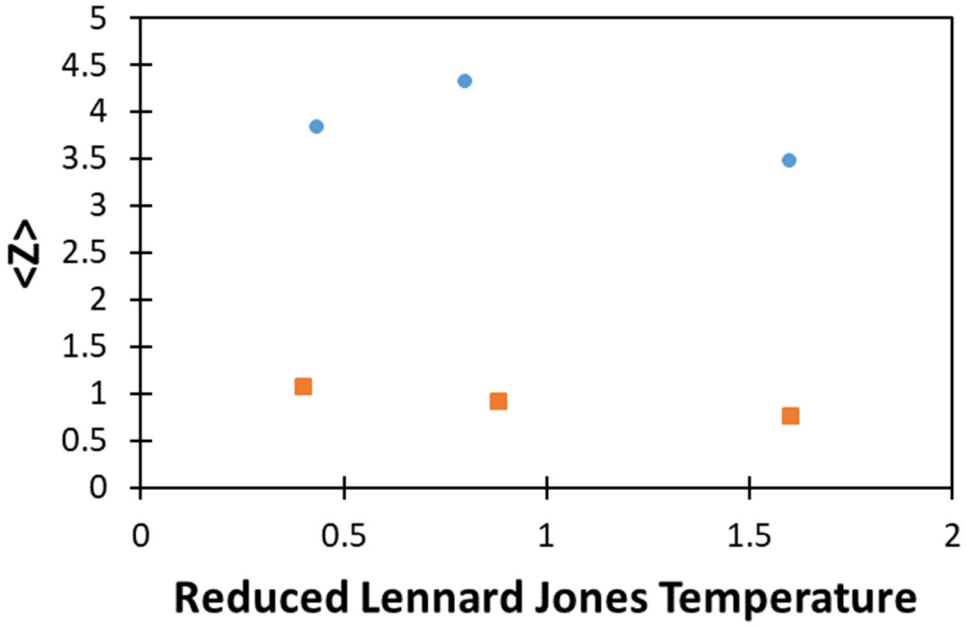

Fig. S14. Average number of entanglements per chain (as computed from the Z1 algorithm[21,22]) vs temperature for the 192-bead chains (blue circles) and the 48-bead chains (orange squares). The lack of an appreciable growth in these values on cooling provides further evidence that topological entanglements are not the origin of the interfacial transient elastomeric effect reported in the main text. The ratio of roughly 4:1 entanglements per chain between the 192-mer and 48 mer chain is consistent with their 4-fold chain length distance and the consistent volumetric entanglement density shown in Fig. S13. The observation of fewer than two entanglements per chain (the percolation transition for crosslinking) in the 48-bead-chain system indicates that it is topologically unentangled, whereas the value of ~4 in the 192-bead-chain system indicates significant topological entanglement.

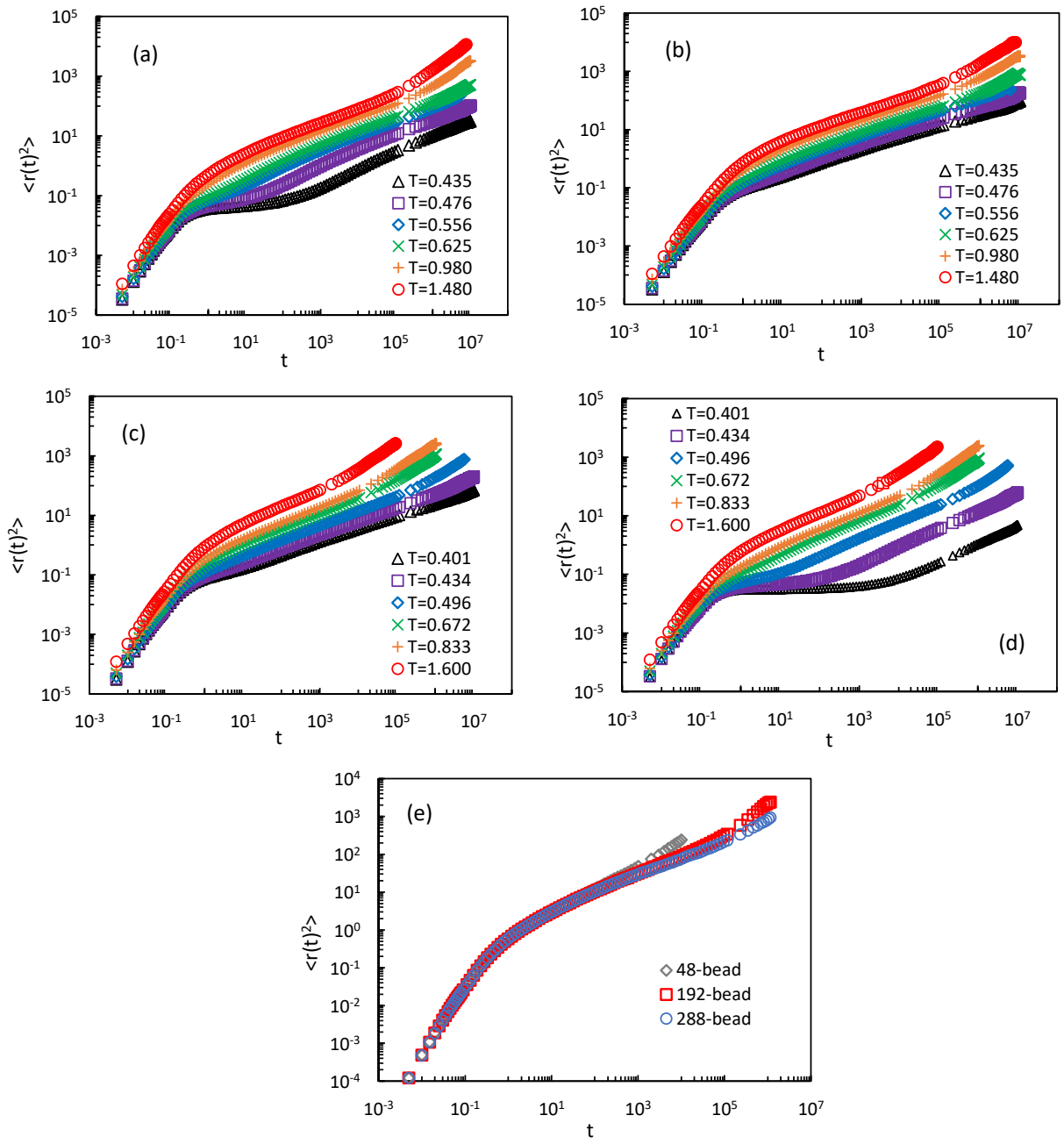

Fig. S15. Raw (unshifted) mean square displacement data corresponding to simulation data shown in figure 3c (a), figure 3d (b), figure 4 (c), figure S10 (d), and figure S12 (e)

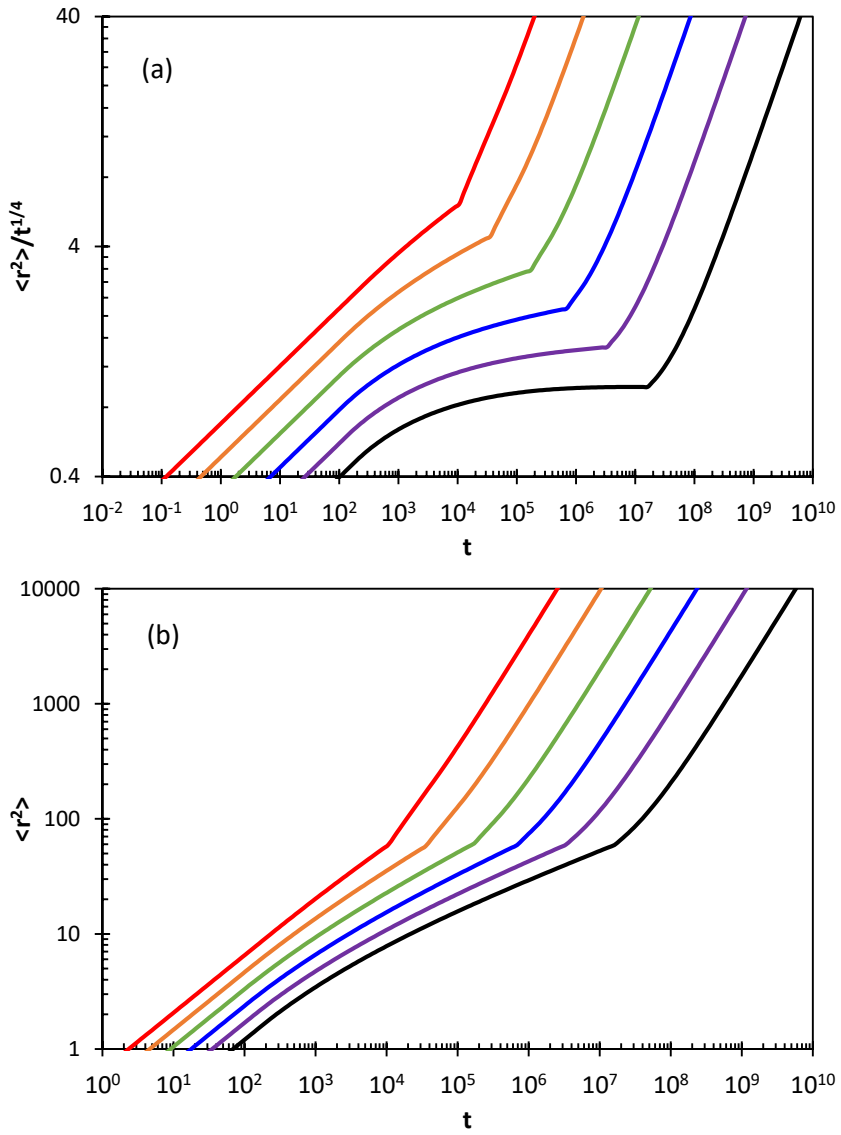

Fig. S16. Raw (unshifted) theoretical predictions of (a) normalized mean square displacement $<r^2>/t^{1/4}$ and (b) non-normalized mean square displacement vs time, for conditions corresponding to the data sets shown in figure 4b. From left to right, curves correspond to bulk relaxation times of 10^0, 10^1, 10^2, 10^3, 10^4, and 10^5 Lennard Jones timesteps.

Supplementary References

1. Schweizer, K. S. & Simmons, D. S. Progress towards a phenomenological picture and theoretical understanding of glassy dynamics and vitrification near interfaces and under nanoconfinement. *Journal of Chemical Physics* **151**, 240901 (2019).
2. Baschnagel, J. & Varnik, F. Computer simulations of supercooled polymer melts in the bulk and in confined geometry. *Journal of Physics: Condensed Matter* **17**, R851–R953 (2005).
3. Peter, S., Meyer, H. & Baschnagel, J. Thickness-dependent reduction of the glass-transition temperature in thin polymer films with a free surface. *J. Polym. Sci. Pt. B-Polym. Phys.* **44**, 2951–2967 (2006).

4. Scheidler, P., Kob, W. & Binder, K. Cooperative motion and growing length scales in supercooled confined liquids. *Europhys. Lett.* **59**, 701–707 (2002).
5. Scheidler, P., Kob, W. & Binder, K. The relaxation dynamics of a confined glassy simple liquid. *Eur. Phys. J. E* **12**, 5–9 (2003).
6. Scheidler, P., Kob, W. & Binder, K. The relaxation dynamics of a supercooled liquid confined by rough walls. *J. Phys. Chem. B* **108**, 6673–6686 (2004).
7. Kob, W., Roldán-Vargas, S. & Berthier, L. Non-monotonic temperature evolution of dynamic correlations in glass-forming liquids. *Nature Physics* **8**, 164–167 (2012).
8. Hocky, G. M., Berthier, L., Kob, W. & Reichman, D. R. Crossovers in the dynamics of supercooled liquids probed by an amorphous wall. *Phys. Rev. E* **89**, 052311 (2014).
9. Kob, W. & Coslovich, D. Nonlinear dynamic response of glass-forming liquids to random pinning. *Phys. Rev. E* **90**, 052305 (2014).
10. Diaz-Vela, D., Hung, J.-H. & Simmons, D. S. Temperature-Independent Rescaling of the Local Activation Barrier Drives Free Surface Nanoconfinement Effects on Segmental-Scale Translational Dynamics near Tg. *ACS Macro Lett.* 1295–1301 (2018) doi:10.1021/acsmacrolett.8b00695.
11. Vela, D., Ghanekarade, A. & Simmons, D. S. Probing the Metrology and Chemistry Dependences of the Onset Condition of Strong 'Nanoconfinement' Effects on Dynamics. *Macromolecules* **53**, 4158–4171 (2020).
12. Khantha, M. & Balakrishnan, V. First passage time distributions for finite one-dimensional random walks. *Pramana - J Phys* **21**, 111–122 (1983).
13. Kremer, K. & Grest, G. S. Molecular dynamics (MD) simulations for polymers. *Journal of Physics: Condensed Matter* **2**, SA295–SA298 (1990).
14. Hanakata, P. Z., Douglas, J. F. & Starr, F. W. Interfacial mobility scale determines the scale of collective motion and relaxation rate in polymer films. *Nature Communications* **5**, 4163 (2014).
15. Hung, J.-H., Patra, T. K., Meenakshisundaram, V., Mangalara, J. H. & Simmons, D. S. Universal localization transition accompanying glass formation: insights from efficient molecular dynamics simulations of diverse supercooled liquids. *Soft Matter* **15**, 1223–1242 (2018).
16. Plimpton, S. J. Fast Parallel Algorithms for Short-Range Molecular Dynamics. *J. Comp. Phys.* **117**, 1–19 (1995).
17. Grest, G. S. Communication: Polymer entanglement dynamics: Role of attractive interactions. *J. Chem. Phys.* **145**, 141101 (2016).
18. Ruan, D. & Simmons, D. S. Roles of chain stiffness and segmental rattling in ionomer glass formation. *Journal of Polymer Science Part B: Polymer Physics* **53**, 1458–1469 (2015).
19. Hiemenz, P. C. & Lodge, T. P. *Polymer Chemistry*. (CRC Press, 2007).
20. Kremer, K. & Grest, G. S. Dynamics of entangled linear polymer melts: A molecular-dynamics simulation. *The Journal of Chemical Physics* **92**, 5057–5086 (1990).
21. Kröger, M. Shortest multiple disconnected path for the analysis of entanglements in two- and three-dimensional polymeric systems. *Computer Physics Communications* **168**, 209–232 (2005).
22. Karayiannis, N. C. & Kröger, M. Combined Molecular Algorithms for the Generation, Equilibration and Topological Analysis of Entangled Polymers: Methodology and Performance. *International Journal of Molecular Sciences* **10**, 5054–5089 (2009).